Bursty Star Formation in Dwarfs is Sensitive to Numerical Choices in Supernova Feedback Models

Eric Zhang[1] , Laura V. Sales[1] , Federico Marinacci[2,3] , Paul Torrey[4] , Mark Vogelsberger[5] , Volker Springel[6] , Hui Li[7] ,
Rüdiger Pakmor[6] , and Thales A. Gutcke[8,9]

[1] Department of Physics and Astronomy, University of California, Riverside, CA 92507, USA
[2] Department of Physics & Astronomy "Augusto Righi," University of Bologna, Via Gobetti 93/2, 40129 Bologna, Italy
[3] INAF, Astrophysics and Space Science Observatory Bologna, Via P. Gobetti 93/3, 40129 Bologna, Italy
[4] Department of Astronomy, University of Virginia, 530 McCormick Road, Charlottesville, VA 22903, USA
[5] Department of Physics, Kavli Institute for Astrophysics and Space Research, Massachusetts Institute of Technology, Cambridge, MA 02139, USA
[6] Max-Planck-Institut für Astrophysik, Karl-Schwarzschild-Straße 1, 85740 Garching bei München, Germany
[7] Department of Astronomy, Tsinghua University, Haidian DS 100084, Beijing, People's Republic of China
[8] Institute for Astronomy, University of Hawaii, 2680 Woodlawn Drive, Honolulu, HI 96822, USA

Abstract

Simulations of galaxy formation are mostly unable to resolve the energy-conserving phase of individual supernova events, having to resort to subgrid models to distribute the energy and momentum resulting from stellar feedback. However, the properties of these simulated galaxies, including the morphology, stellar mass formed, and the burstiness of the star formation history, are highly sensitive to the numerical choices adopted in these subgrid models. Using the SMUGGLE stellar feedback model, we carry out idealized simulations of an $M_{\rm vir} \sim 10^{10}\, M_\odot$ dwarf galaxy, a regime where most simulation codes predict significant burstiness in star formation, resulting in strong gas flows that lead to the formation of dark matter cores. We find that by varying only the directional distribution of momentum imparted from supernovae to the surrounding gas, while holding the total momentum per supernova constant, bursty star formation may be amplified or completely suppressed, and the total stellar mass formed can vary by as much as a factor of $\sim$3. In particular, when momentum is primarily directed perpendicular to the gas disk, less bursty and lower overall star formation rates result, yielding less gas turbulence, more disky morphologies, and a retention of cuspy dark matter density profiles. An improved understanding of the nonlinear coupling of stellar feedback into inhomogeneous gaseous media is thus needed to make robust predictions for stellar morphologies and dark matter core formation in dwarfs independent of uncertain numerical choices in the baryonic treatment.

Unified Astronomy Thesaurus concepts: Galaxy structure (622); Starburst galaxies (1570); Dwarf galaxies (416); Galaxy evolution (594); Star formation (1569); Galaxy dark matter halos (1880); Computational methods (1965)

1. Introduction

Galaxy formation at the scale of dwarfs ($M_* \sim 10^6$–$10^9\, M_\odot$) is extremely inefficient, turning only a small fraction of the available gas into stars ($\sim$10%; e.g., C. Conroy & R. H. Wechsler 2009; B. P. Moster et al. 2013; P. Behroozi et al. 2019). One of the most important processes affecting the formation of stars in dwarf galaxies are supernovae (SNe), which deposit a significant amount of energy into the interstellar medium (ISM; e.g., R. B. Larson 1974; J. F. Navarro & S. D. M. White 1993; O. Agertz et al. 2013). This energy deposition is instrumental in regulating the rate of star formation in galaxies of all masses to the observed levels (e.g., O. Agertz et al. 2010; J. Guedes et al. 2011; P. F. Hopkins et al. 2011; M. Aumer et al. 2013; A. Gatto et al. 2016). On the scale of dwarfs, SN energy coupled efficiently to the ISM may also be responsible for generating fluctuating gravitational potentials that result in the redistribution of dark matter from the center to the outer regions of the galaxy and the formation of constant density

cores (e.g., J. F. Navarro et al. 1996a; A. Pontzen & F. Governato 2012; A. Di Cintio et al. 2014; A. A. Dutton et al. 2016; K. El-Badry et al. 2016; J. I. Read et al. 2016; E. Tollet et al. 2016; J. Freundlich et al. 2020; E. D. Jahn et al. 2023; B. Azartash-Namin et al. 2024).

In practice, an SN event can be modeled as a point injection of a large amount of thermal energy, which expands as a shock into its environment. The first stage of this expansion is energy conserving, as the thermal pressure inside the shock drives the bubble's expansion according to the Sedov–Taylor solution (e.g., G. I. Taylor 1950; L. I. Sedov 1959). Once the shock slows down and the driving pressure becomes comparable to the ambient pressure, the bubble enters the snow-plow or momentum-conserving phase, where the swept up matter continues to move without being subject to external forces.

However, it is very difficult for simulations to accurately capture the way in which SN explosions expand into the ISM (e.g., C. Scannapieco et al. 2012). First, the Sedov–Taylor solution, and related SN feedback models (e.g., R. A. Chevalier 1974; D. F. Cioffi et al. 1988; B. T. Draine & D. T. Woods 1991; K. Thornton et al. 1998), invoke a number of simplifying assumptions—in particular, they are derived based on a homogeneous local ISM at rest. However, neither of these assumptions are necessarily true for SNe in galaxies; the local ISM may be inhomogeneous on a wide range of scales, including scales comparable to the size of the blast wave itself.

---

[9] NASA Hubble Fellow.

It will also often not be at rest, and in many cases we should expect the gas to be moving away from active star-forming areas, due to previous SN events or the action of stellar winds. Furthermore, the resolution of simulations is often insufficient to explicitly capture the relevant physics of the SN blast wave. The time resolution needed to resolve the radiative cooling of very hot gas after a point injection of thermal energy is difficult to reach in galaxy formation simulations, leading to what is known as the "overcooling problem" (e.g., N. Katz 1992; M. C. Smith et al. 2018; M. Vogelsberger et al. 2020), in which, due to purely numerical errors, the thermal energy injected by SNe dissipates too quickly to expand as a shock into the ISM. Often, the spatial resolution is also too coarse to individually resolve the energy-conserving and momentum-conserving phases of the expanding shock. Typical cooling radii, or the size of the bubble at the onset of the momentum-conserving phase, span from ∼parsec scale to a few hundred parsecs, depending on the local conditions of the ISM. This is often smaller than the spatial resolution of galaxy-scale numerical simulations, leaving the energy-conserving phase unresolved.

As such, SN feedback is often implemented as a subgrid process. Methods include modified thermal injection schemes (e.g., G. Murante et al. 2010; C. Dalla Vecchia & J. Schaye 2012; E. Chaikin et al. 2023), directly injecting momentum into the ISM (e.g., J. F. Navarro & S. D. M. White 1993; J. C. Mihos & L. Hernquist 1994; M. Vogelsberger et al. 2013; P. F. Hopkins et al. 2018a), temporarily disabling radiative cooling after SN events (e.g., G. Stinson et al. 2006; O. Agertz et al. 2010; R. Teyssier et al. 2013), modeling clusters of multiple SNe collectively as an expanding superbubble (e.g., B. W. Keller et al. 2014; K. El-Badry et al. 2019), or resorting to smoothly representing the ISM by means of an effective equation of state (V. Springel & L. Hernquist 2003). Several current subgrid SN models based on direct moment injection have begun to explicitly compensate for resolution limitations by injecting the terminal momentum of the SN ejecta after the unresolved Sedov–Taylor phase, accounting in the calculation for various dependencies including local gas density and metallicity (e.g., C.-G. Kim & E. C. Ostriker 2015; P. F. Hopkins et al. 2018a; F. Marinacci et al. 2019; J. M. Pittard 2019; P. I. Karpov et al. 2020). Notably, FIRE-3 (P. F. Hopkins et al. 2023) adjusts the momentum injected also for instances when the medium is not at rest, in an attempt for a more physically motivated model. In general, higher order considerations and more detailed subgrid treatments may be advisable (P. F. Hopkins 2024).

Recently, some simulations have reached the ultrahigh resolution needed to model SNe via direct injection of thermal energy (e.g., A. Emerick et al. 2019; C.-Y. Hu 2019; N. Lahén et al. 2020; T. A. Gutcke et al. 2021; Y. Deng et al. 2024), and can thus explicitly resolve the expansion of SN bubbles into realistic, inhomogeneous ISM structures. At these resolutions, the momentum injection into the ISM will naturally arise from thermal expansion, and will thus not rely on arbitrary numerical choices. However, these resolutions are not yet achievable in large-scale simulations. The reality of SN injection in galaxy formation simulations is, likely, substantially more complex than assumed in the prescriptions used, mostly due to the (unresolved) inhomogeneities in the ISM of galaxies.

For example, even a modestly low density of $n \sim 0.01$ particles cm^{-3} corresponds to a cooling radius of about 200 pc, which is often comparable to the size of superbubbles formed by clustered SN feedback (e.g., C. Li et al. 2024). Studies using small-scale simulations of a more realistic inhomogeneous ISM (e.g., D. Martizzi et al. 2015) have shown departures in the evolution of the SN remnants from the traditionally assumed subgrid models that rest on assumptions of spherically symmetric expansion into a homogeneous media. The propagation speed and momentum coupling of the SN energy vary along low- and high-density channels within the structured ISM, contributing to the departure from idealized solutions in homogeneous media. On a macroscopic level, for stratified media (such as the disk of galaxies) this can result in preferential coupling of the energy and momentum for different directions, which might not be properly taken into account when enforcing symmetric energy–momentum deposition in subgrid models.

It is necessary to produce accurate subgrid models of SN feedback since many of the predicted properties of simulated galaxies may show variations depending on the details of the baryonic treatment and, in particular, the stellar feedback implementation (L. V. Sales et al. 2010; C. Scannapieco et al. 2012; E. Chaikin et al. 2022). This is particularly true in the regime of dwarf galaxies, where the relatively shallower gravitational potential makes the system more responsive to the energy and momentum input from feedback. There is consensus in the field that stellar feedback, and mostly SNe, are capable of regulating star formation in dwarf galaxies to observed levels, by disrupting cold, dense gas clumps that would form far too many stars compared to observations if not regulated by feedback (e.g., see the comparison of several codes in L. V. Sales et al. 2022). However, there is less agreement on the level of "burstiness" that is reasonable to expect in the regime of dwarfs, and whether theoretical models compare well with observational constraints (e.g., M. Sparre et al. 2017; S. G. Patel et al. 2018; N. Emami et al. 2019, 2021).

If star formation is indeed as bursty as predicted by some of the state-of-the-art numerical simulations, this carries important consequences for the theoretical predictions of the stellar sizes, morphologies, and inner dark matter distribution in dwarf galaxies. If gas contributes sufficiently to the local density in the inner regions of halos, which may occur in the case of gas-rich dwarfs, bursty episodes of star formation can generate substantial gas flows that create fluctuating gravitational potentials in the inner regions of low mass halos combined with powerful outflows (e.g., M. C. Smith et al. 2021). These quick (i.e., on subdynamical timescales) fluctuations in the gravitational potential of the galaxy result in a net gain of energy for collisionless components like stars and dark matter, making them less tightly bound, and thus they tend to migrate outwards (J. F. Navarro et al. 1996a; A. Pontzen & F. Governato 2012; A. Benitez-Llambay et al. 2019). Shallower distributions of stars and dark matter are thus expected in systems where star formation is bursty and stellar feedback is efficiently coupled to the surrounding ISM, including a transformation from cuspy dark matter halos into cored ones. Through this process, numerical details on the subgrid modeling of star formation and stellar feedback have a direct impact on cosmological predictions and our understanding of cold dark matter (CDM) as a plausible dark matter model.

In this paper, we revisit the assumption of an isotropic deposition of SN momentum for subgrid models of feedback using the multiphase SMUGGLE model (e.g., F. Marinacci et al. 2019) applied in simulations of an isolated dwarf halo. In

Section 2 we discuss the simulation setup and the methods used to control both: (i) directional anisotropy and (ii) cell weighting scheme of the SN feedback model. In Sections 3 and 4 we present our main results on how varying these two assumptions may impact the large-scale dwarf properties, including their star formation histories, morphologies, and inner dark matter distributions. In Section 5 we summarize our results.

2. Description of the Simulations

We use the moving-mesh hydrodynamics code AREPO (V. Springel 2010) to run simulations of an isolated $M_{\rm vir} \sim 10^{10}\ M_\odot$, $M_* \sim 10^8\ M_\odot$ dwarf galaxy where the virial quantities are defined within a radius that encloses an average density of 200 times the critical density of the Universe. Our runs have a reference resolution with $\sim$6000 $M_\odot$ for the baryonic component (gas and stars) and $\sim$25,000 $M_\odot$ for the dark matter particles. A gravitational softening length of 32 pc is used for every particle. Stars form by transforming an eligible gas cell into a single star, which means that initially stars have the same mass as the parent gas cell. The mesh refinement scheme implemented in AREPO ensures that the mass of any given gas cell is within a factor of 2 from this reference resolution. Hence, star particles are formed at around this particle mass; however, due to mass loss in stellar feedback processes, star particle masses may decrease below this value; for example, in our default runs we find that the average stellar particle mass falls to $5000 \pm 1500\ M_\odot$ by the end of the simulation (where the uncertainty corresponds to the rms of the stellar particle mass distribution.) We test convergence of the results using a $\times 10$ better resolution run in the Appendix.

The initial conditions consist of a gas-rich disk ($M_{\rm gas} \sim 5 \times 10^8\ M_\odot$) in hydrostatic equilibrium with the dark matter halo, with an additional population of old disk stars ($M \sim 7 \times 10^7\ M_\odot$) and old bulge stars ($M \sim 5 \times 10^6\ M_\odot$). The initial dark matter halo is a Navarro–Frenk–White (NFW; J. F. Navarro et al. 1996b) profile with concentration $c = 15$, the initial gas and stellar disks are in an exponential profile, and the initial stellar bulge is an L. Hernquist (1990) profile. This setup is similar to those presented in P. F. Hopkins et al. (2011), J. D. Burger et al. (2022a, 2022b), and E. D. Jahn et al. (2023). The galaxy lies at the center of a 3D box with 200 kpc on a side. All simulations are run for at least 2 Gyr, with a snapshot saved every 5 Myr. All galaxy-wide properties discussed within this work are calculated from all snapshots over the first 2 Gyr, unless stated otherwise.

We briefly summarize the SMUGGLE stellar feedback model as per F. Marinacci et al. (2019, hereafter M19). It includes various processes of star formation, stellar feedback, and the heating and cooling of gas. Star formation is primarily modulated by two numerical parameters: the star formation efficiency $\epsilon_{\rm SF}$, which regulates the rate at which a given gas cell forms stars, and a density threshold $\rho_{\rm th}$, which gas cells are required to exceed in order to form stars. Chief among the relevant feedback mechanisms, and the one we will focus on in this paper, is the feedback done by SNe.

The main parameters involved in the star formation and feedback modeling are summarized in Table 1. Our findings are robust to a range of numerical choices, which is presented in the Appendix.

Table 1
List of the Numerical Parameters and Initial Conditions Used in the Simulations

Parameter	Value
Halo Virial Mass	$1 \times 10^{10}\ M_\odot$
Disk Stellar Mass (Initial)	$7 \times 10^7\ M_\odot$
Bulge Stellar Mass (Initial)	$5 \times 10^6\ M_\odot$
Gas Mass (Initial)	$5 \times 10^8\ M_\odot$
Target Baryonic Mass	$6000\ M_\odot$
Dark Matter Particle Mass	$25{,}000\ M_\odot$
Softening Radius (All Particles)	32 pc
Star Formation Efficiency	0.01
Star Formation Density Threshold	$100\ m_{\rm H}\ {\rm cm}^{-3}$

2.1. Star Formation Prescription

To model star formation, gas cell are converted into star particles, probabilistically, at a rate consistent with

$$\dot{M}_{\rm SF} = \epsilon_{\rm SF} \frac{M_{\rm cell}}{t_{\rm dyn}}, \qquad (1)$$

where $\epsilon_{\rm SF}$ is the star formation efficiency, which is a tunable dimensionless factor which we set to 0.01 (M19; in accordance with M. R. Krumholz & J. C. Tan 2007), $M_{\rm cell}$ is the mass of the gas cell, and $t_{\rm dyn}$ is the dynamical timescale of the gas within the cell, given by

$$t_{\rm dyn} = \sqrt{\frac{3\pi}{32 G \rho_{\rm cell}}}, \qquad (2)$$

where G is the gravitational constant and $\rho_{\rm cell}$ is the density of the gas cell.

Additionally, gas cells must be sufficiently dense in order to form stars; this is enforced by allowing only gas cells with a density $\rho_{\rm cell} > \rho_{\rm th}$ to become a star particle. In the main body of this work, we set $\rho_{\rm th}$ to be 100 particles cm^{-3}. The SMUGGLE model also requires that the gas is locally gravitationally bound in order to form stars; this is modeled by a virial parameter criterion for each gas cell, described in M19; only gas cells satisfying this criterion are eligible to become a star particle.

At the time of formation, star particles keep the mass, position, and velocity of their progenitor gas cells. Each star particle represents a stellar population, consistent with a G. Chabrier (2003) initial mass function, which evolves coevally according to the model described in M19.[10]

2.2. Supernova Feedback

SN events occur according to the stellar population evolution model described in M19, in which Type II or Ia SNe occur in a star particle according to the ages of OB and white dwarf stars within a given stellar population. SNe are resolved discretely; typically, at the resolution of our simulations, no more than one SN occurs within a star particle at any given time step.

At each SN event, a nominal energy of

$$E_{\rm tot} = n_{\rm SN} E_{51}, \qquad (3)$$

---

[10] For the mass resolutions within this work, the masses of star particles are sufficiently high that each particle can be treated as a stellar population that samples well the initial mass function.

is released by a star particle into the neighboring gas particles where n_{SN} is the number of SNe occurring within the numerical event, and $E_{51} = 1.0 \times 10^{51}$ erg. This energy is entirely converted into a scalar momentum, via

$$p_{tot} = \sqrt{2 m_{tot} E_{tot}}, \qquad (4)$$

where m_{tot} is the total mass of the SN ejecta. This linear momentum is then partitioned among the nearest $N_{ngb} = 32$ gas cells, according to a weight factor w_i for each neighboring cell, indexed by i. Then, the (nominal) linear momentum injected into each neighbor gas cell is

$$\tilde{p}_i = \frac{p_{tot} w_i}{\sum_i w_i}, \qquad (5)$$

so that, in principle, the sum of all linear momenta entering the gas cells is p_{tot}. However, a number of numerical postprocessing procedures are applied before imparting the momentum to a gas cell. First, due to the unresolved nature of the energy-conserving phase of the SN blast wave in these simulations, the linear momentum injected into a gas cell i by a star particle is boosted[11] (in a manner consistent with P. F. Hopkins et al. 2018a) by a factor

$$\beta = \min\left(\sqrt{1 + \frac{m_i}{\delta m_i}}, \frac{p_{term}}{p_{tot}}\right), \qquad (6)$$

where m_i is the mass of the target gas cell, $\delta m_i = m_{tot} w_i / \sum_i w_i$ is the mass of the ejecta entering the gas cell, and p_{term} is the terminal momentum of the SN shock, which is (in accordance with D. F. Cioffi et al. 1988, and used by M19), given by

$$p_{term} = 4.8 \times 10^5 \, M_\odot \, \text{km s}^{-1} \cdot \bar{E}^{13/14} \bar{n}^{-1/7} f(Z), \qquad (7)$$

where $\bar{E}$ is the total energy released in units of 10^{51} erg, $\bar{n}$ is the local density estimate in units of particles cm^{-3}, and

$$f(Z) = \min\left[\left(\frac{Z}{Z_\odot}\right)^{-0.14}, 2\right]^{3/2}, \qquad (8)$$

where Z is the metallicity, which for simplicity is set to the solar value ($Z_\odot$). The inclusion of the minimum function in Equation (6) ensures that even when the SN momentum is boosted, the total momentum injected does not exceed the maximum possible momentum injected. The actual linear momentum injected into a gas cell is then

$$p_i = \beta \tilde{p}_i. \qquad (9)$$

Furthermore, the nearest N_{ngb} neighboring gas cells are sometimes too far away from the star particle for momentum injection to be considered physical. To prevent star particles from being able to affect faraway gas cells, a "superbubble limiter radius" of $r_{SB} = 1024$ pc is imposed on all star particles, preventing momentum from being injected into gas cells further than this radius.[12]

---

[11] Due to the typical value of p_{term} given in Equation (7), this value is in practice always greater than 1.
[12] M19 verify that varying this radius within a large range of values does not change the results.
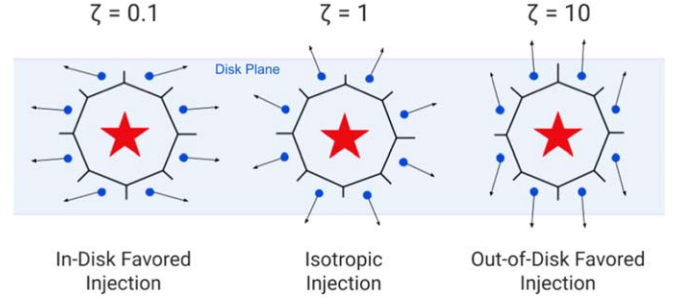

Figure 1. Picture of the anisotropic SN momentum injection scheme, as parameterized by the nominal anisotropy factor ζ. The star particle undergoing an SN event is shown in red, and the surrounding gas cells are shown as blue circles. The arrows indicate the magnitude and direction of the momentum injection. A low ζ value injects momentum primarily within the disk plane, and a high ζ injects momentum primarily out of the disk plane. $\zeta = 1$ implies isotropic injection. Note that only the direction of injected momenta varies with ζ; the magnitude does not.

The default choice for the weight is the solid angle of opening Ω_i, defined by

$$\Omega_i = 2\pi \left\{ 1 - \frac{1}{[1 + A_i/(\pi |r_i - r_*|^2)]^{1/2}} \right\}, \qquad (10)$$

where A_i is the cell boundary area. Note that this weighting scheme follows that in other models, such as FIRE (see Equation (2) in P. F. Hopkins et al. 2018a). However, other choices for the cell weights are possible, such as the kernel-weighted cell volume $w_i = W_i V_i$ and the kernel-weighted cell mass $w_i = W_i m_i$ (where V_i is the volume of the target gas cell and $W_i = W(|r_i - r_*|, h)$ is the standard cubic spline smoothed particle hydrodynamics kernel value).

The weight factor w_i controls the magnitude of momentum that each gas cell receives. The direction of this momentum injection can then independently be determined by the nominal anisotropy factor, ζ. In particular, we control the vector momentum injected into each gas cell according to an anisotropic direction vector k, such that the momentum δp_i delivered to the gas particle is

$$\delta p_i = \frac{p_i k}{|k|}, \qquad (11)$$

where the anisotropic direction vector k is defined by

$$k = [x_i - x_*, y_i - y_*, \zeta(z_i - z_*)], \qquad (12)$$

where (x_i, y_i, z_i) is the position of the target gas particle and (x_*, y_*, z_*) is the position of the star particle doing the feedback. According to this formula, the relative amount of momentum being injected in the z-direction is controlled by the factor ζ. We show a picture of this injection scheme in Figure 1.

A higher ζ means more momentum is being injected in the z-direction, but the normalization factors ensure that the magnitude of momentum released into a particular gas cell is independent of ζ. $\zeta = 1$ implies isotropic injection; that is, the momentum injected into the cell will always point radially away from the source star particle. ζ can only change the direction of the injected momentum; for any given cell, the magnitude of momentum injected into it is not affected by the choice of ζ; it is only controlled by the cell weighting scheme w_i and boost factor β.
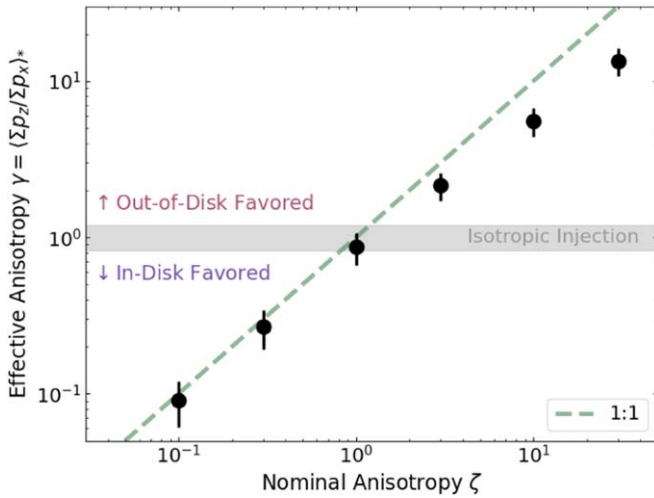
Figure 2. The effective anisotropy (γ, as defined in Equation (13)), and its associated uncertainty, as a function of the nominal anisotropy (ζ, as defined in Equations (11) and (12)). The nominal anisotropy controls the ratio of momentum injected in the polar (z) direction to the in-plane (x, y) directions, by every star particle, before postprocessing effects are considered. The effective anisotropy measures the ratio between the total momenta actually injected in these directions.

As mentioned before, some postprocessing calculations may affect the final momentum injected into the cell after the weight and direction has been defined. This occurs due to variations in the distribution of gas cells about star particles, which can affect the boost factor (Equation (6)) and superbubble limiter. As a result, the nominal anisotropy ζ may be different from the effective anisotropy imparted to the individual cells. We quantify the true anisotropy in momentum injection by an effective anisotropy factor, γ, which we define by the ratio of the total momentum injected into gas by SNe along the z-axis (regardless of the positive or negative direction), to the total momentum injected along the x-axis[13]

$$\gamma = \left\langle \frac{\sum_{\mathrm{SNe}}\sum_i \delta p_{i,z}}{\sum_{\mathrm{SNe}}\sum_i \delta p_{i,x}} \right\rangle_{\mathrm{stars}}. \quad (13)$$

In practice, this factor does not need to be equal to the nominal anisotropy factor ζ. However, Figure 2 indicates that γ does in fact scale well with ζ, so that the degree of anisotropy is still reliably controlled by ζ. Furthermore, γ carries an associated uncertainty, which is the standard deviation of the quantity averaged over all star particles in Equation (13).

Thus, we explore the effect of anisotropy by varying ζ, and we label our runs by the value of ζ we employ for that run. However, we will measure all properties in terms of the effective anisotropy, γ. Changes in the cell weighting scheme will also be discussed. Table 2 shows a list of all runs covered in the main body of this paper, the value of ζ used, and the resulting value of γ for the corresponding simulation.

In theory, differing distributions of gas cells around star particles throughout the runs can lead to some variation in the total magnitude of momentum being injected by a typical star particle between runs. In this case, we would be unable to conclude that differences in the dwarf properties are purely due to a change in the directional distribution of momentum.

However, we do find that, for the same choice of cell weighting scheme, w_i, varying the anisotropy factor does not change the typical momentum released and imparted to surrounding cells by a star particle[14] to any significant degree. However, between different cell weighting schemes, the total momentum injected can differ by more than half an order of magnitude. We examine the effect of the cell weighting scheme in more detail in Section 4.

2.3. Other Physical Processes Involved in SMUGGLE

In addition to SN feedback, the SMUGGLE model includes other forms of stellar feedback, including OB and AGB stellar winds, radiation pressure, and photoionization of nearby gas. These modes of stellar feedback are energetically subdominant (M19, Figure 13), but can be important for preprocessing gas before SNe go off. Photoionization, in particular, is a crucial process in regulating star formation by disrupting star-forming gas clumps (e.g., M. C. Smith et al. 2021); it is enabled in our simulations, though we do not explicitly study its effects in this work. Also included are radiative heating and cooling mechanisms of the ISM gas, including cooling of H, He, and metals down to 10 K, self-shielding from ionizing UV radiation, cosmic-ray heating, and photoelectric heating. The parameterization of these additional feedback processes do not change across different runs, so the only variation between the runs considered in this work are those of the SN feedback.

3. Anisotropic Momentum Injection

We explore the effects of varying the subgrid SN momentum injection scheme. In this section, we focus on the effects of changing the directionality of the momentum injection. As introduced in Section 2 and Equation (13), the anisotropy in SN momentum injection is quantified by γ, where $\gamma = 1$ indicates isotropic injection, and a γ of greater (less) than 1 indicates momentum primarily being injected perpendicular to (within) the plane of the disk. We will focus on three runs in this section: *zeta0.1* (in-disk favored injection), *zeta1* (isotropic injection, default SMUGGLE choice), and *zeta10* (out-of-disk favored injection). Where possible we will refer to specific runs by their descriptive indicators (i.e., "isotropic" for "*zeta1*"). Each galaxy is followed for at least 2 Gyr.

3.1. Star Formation History

Of particular interest is the effect on the star formation history and its burstiness. A bursty star formation history can determine the mass, size and morphology of dwarfs, along with their dark matter distribution (e.g., G. S. Stinson et al. 2007; A. Pontzen & F. Governato 2012; A. Di Cintio et al. 2014; A. González-Samaniego et al. 2014; K. El-Badry et al. 2016; M. Sparre et al. 2017). We plot the star formation histories of the in-disk favored (*zeta0.1*), isotropic (*zeta1*), and out-of-disk favored (*zeta10*) injection runs in Figure 3.

Qualitatively, in-disk favored (green curve) and isotropic injection (purple curve) are associated with bursty star formation histories, as seen by the prevalence of sharp peaks in their SFR curves; contrarily, out-of-disk favored injection (orange curve) leads to a smoother star formation history.

---

[13] It would also be valid to use the y-axis for this definition, since it is also within the disk plane; however, we will choose to use the x-axis.

[14] Since the momentum injected is measured on a per star particle basis, it will depend on the simulation mass resolution as well. We do not consider this dependence in this work, since we use the same mass resolution for all simulations in the main body of this work.

<div align="center">

Table 2
List of the Simulations and the Parameters Used in Each

</div>

Simulation Name	Nominal SNe Anisotropy ζ	Effective SNe Anisotropy γ	SN Cell Weight Scheme w_i	log10 M_* Formed ($M_\odot$)
zeta0.1 (In-disk Favored)	0.1	0.091 ± 0.030	Solid Angle (Ω)	7.80
zeta0.3	0.3	0.27 ± 0.08	Solid Angle (Ω)	7.71
zeta1 (Isotropic)	1.0	0.87 ± 0.20	Solid Angle (Ω)	7.71
zeta3	3.0	2.2 ± 0.4	Solid Angle (Ω)	7.58
zeta10 (Out-of-disk Favored)	10.0	5.6 ± 1.1	Solid Angle (Ω)	7.38
zeta30	30.0	13 ± 3	Solid Angle (Ω)	7.32
zeta1-VolWgt	1.0	0.90 ± 0.23	Kernel-weighted Volume	7.81
zeta10-VolWgt	10.0	5.4 ± 1.4	Kernel-weighted Volume	7.62
zeta1-MassWgt	1.0	0.95 ± 0.30	Kernel-weighted Mass	7.36
zeta10-MassWgt	10.0	5.6 ± 1.9	Kernel-weighted Mass	7.37

Note. Simulations are named by the value of *zeta* (ζ) and the cell weighting scheme used for that run, but we will quantify any physical properties by their dependence on the effective anisotropy γ, and its associated uncertainty. M_* formed refers to the total stellar mass formed within the entire simulation volume, by the final simulation time of 2 Gyr.

We quantify the burstiness of a run by the parameter

$$B = \frac{\sigma(\langle \text{SFR} \rangle_{\tau_{\text{avg}}}(t))}{\langle \text{SFR} \rangle}, \qquad (14)$$

where B stands for the burstiness, $\langle \text{SFR} \rangle_{\tau_{\text{avg}}}(t)$ denotes the rolling average of the SFR over an interval τ_{avg}, σ denotes the standard deviation of the time series, and $\langle \text{SFR} \rangle$ is the average SFR of the simulation. The averaging over short timescales (5, 10, and 25 Myr) ensure that rapid random fluctuations in the SFR, which do not affect large-scale movement of gas due to feedback, are not counted as additional burstiness.

In Figure 4, we show the dependence of the burstiness on the anisotropy factor γ for various averaging durations $\tau_{\text{avg}} = 5$, 10, and 25 Myr. Using this metric, we find that for any choice of τ_{avg} within this range, isotropic runs with lower γ have bursty star formation histories, and runs with $\gamma > 1$ have substantially less bursty star formation histories. These findings are robust to several free parameters of the simulation including the density threshold for star formation, the star formation efficiency, and the numerical resolution (see the Appendix for details).

We also show the dependence of the total stellar mass on γ in the top panel of Figure 4 and find that a preferentially off-plane momentum injection (higher γ) is associated with a lower stellar mass. The effect is noticeable, with the final stellar mass differing by roughly half an order of magnitude between the highest and lowest anisotropy factors considered. From this, we conclude that out-of-disk momentum injection is associated with a less bursty and lower overall rate of star formation.

3.2. Gas Morphology and Bulk Motions

The increased burstiness seen in runs with the isotropic or in-disk favored momentum injection can be explained by differences in how bulk gas flows within the gas disk are induced by the SN momentum injection. We consider the flows generated parallel to the disk, or in the radial direction, defined by

$$\dot{M}_R = \frac{1}{L} \int dm \, \boldsymbol{v} \cdot \hat{\boldsymbol{R}}, \qquad (15)$$

where $\hat{R}$ refers to the unit vector of the 2D cylindrical radial coordinate, and flows generated perpendicular to the disk, or in the vertical direction, defined by

$$\dot{M}_z = \frac{1}{L} \int dm \, \boldsymbol{v} \cdot \pm \hat{z}. \qquad (16)$$

Here $\boldsymbol{v}$ is the velocity of the gas, and the integrals are taken over thin shells of thickness $L = 50$ pc, centered about the surface of a cylinder with diameter 2 kpc (radius 1 kpc) and height 0.5 kpc (0.25 kpc above and below the center), centered about the center of mass of all star particles. In Figure 5, we show a diagram of the cylinder of interest (left), and the mass flux rates of gas across the shell (right). For the in-disk favored (*zeta0.1*, top right), isotropic (*zeta1*, middle right), and out-of-disk favored (*zeta10*, bottom right) runs, the radial (parallel to the disk plane) gas mass flux rates are shown in blue, and the vertical (perpendicular to the disk plane) gas mass flux rates are shown in green. To study the way star formation episodes affect these bulk flows, these mass flux rates are compared to the SFR in the cylinder's interior, shown in red.

Since the gaseous disk extends to a diameter of roughly 8 kpc, the cylindrical region in question is deeply embedded inside the disk. Thus, the rates calculated in Equations (15) and (16) trace large-scale flows within the disk, rather than outflows. Typically, the cylinder roughly encloses 50% of the stellar mass and 5%–20% of the baryonic mass of the galaxy, with lower baryonic fractions occurring during intense outflow episodes, where the gas is temporarily expelled from the central regions.

In the top and middle panels, we find that in the in-disk favored and isotropic runs, a significant proportion of the momentum is injected within the plane of the disk, leading to large amounts of gas being moved in bulk flows parallel to the disk plane. These bulk gas flows inside the disk can also drive additional star formation bursts due to gas compression, leading to additional stars being formed in these runs, and driving instability within the disk, perpetuating the cycle of radially outward gas motions and bursty star formation. Note the clear correlation between the inward gas motions (dips in the blue and green curves in Figure 5), star formation activity (peaks in the red curve), and the subsequent outward gas motion (peaks in the blue curve). The timing of the starbursts is consistent with those predicted in E. Cenci et al. (2023), who
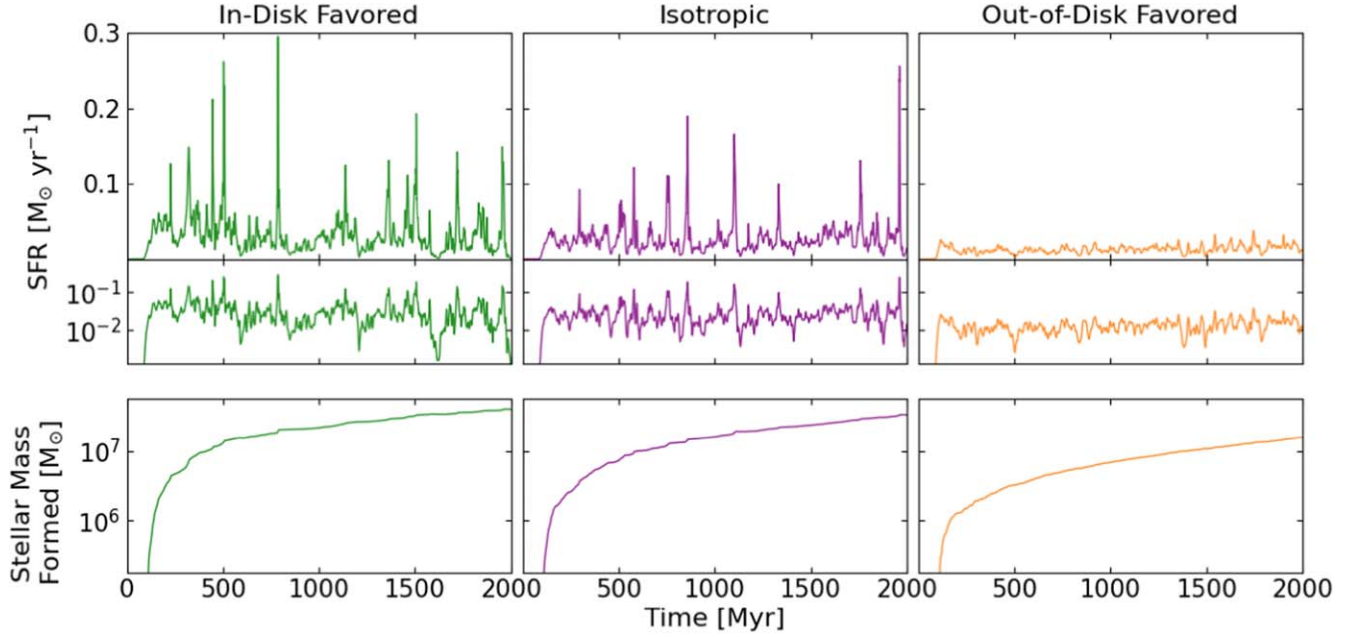
Figure 3. Star formation histories of the entire galaxy in the in-disk favored (green, left), isotropic (purple, center), and out-of-disk favored (orange, right) momentum injection runs. The top row shows the star formation rate (SFR) in linear scale, the middle row shows the SFR in log scale, and the bottom row shows the cumulative stellar mass formed. The burstiness of the SFR depends substantially on the injection model, with the in-disk favored and isotropic models resulting in more bursty histories and a greater stellar mass than the out-of-disk favored model.
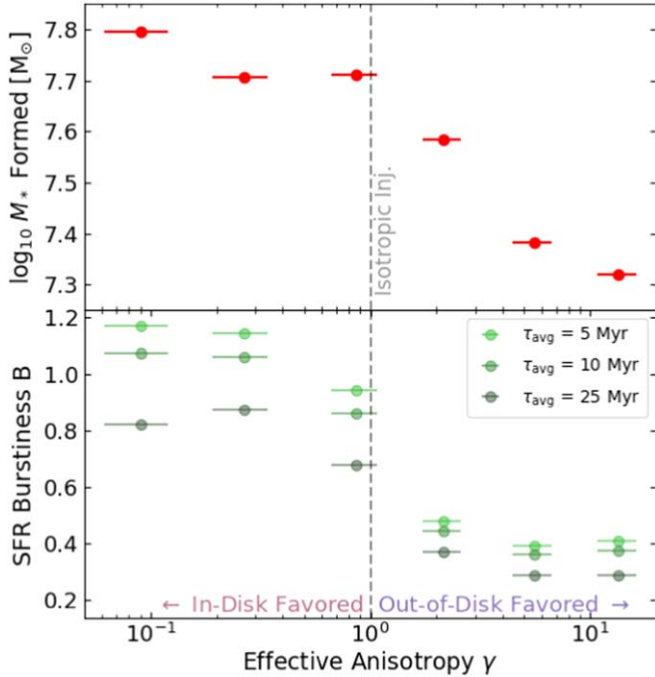
Figure 4. Top: total stellar mass formed. Higher-γ runs (i.e., runs with more momentum directed outside the disk), form a lower total stellar mass. The difference in the stellar mass formed can vary by up to half an order of magnitude, across all runs considered. Bottom: burstiness parameter B as defined by Equation (14). Higher-γ runs tend to be less bursty according to this parameter, over a wide range of SFR averaging timescales. The horizontal error bars are the uncertainties in γ, as discussed in Equation (13) and Table 2.

state that a centrally concentrated gas distribution in a dwarf is a good indicator that a starburst will occur. Outflow episodes occur quite rapidly, with the blue and green peaks lasting ~25 Myr (compared to an orbital timescale of ~125 Myr at the cylinder's radius).

Conversely, in the out-of-disk favored run (bottom panel), the momentum is primarily injected outside the disk, so that gas compression induced by bulk radial flows is less prevalent, along with a less bursty star formation history. This indicates that radial, not vertical, gas flows are primarily responsible for driving additional star formation and turbulence. Interestingly, even though the SNe do not lead to a bursty SFR or large-scale gas flows in the out-of-disk favored run, the stellar feedback is still capable of regulating SFR to similar or lower levels than the isotropic or in-disk injection runs. Thus, neither bursty star formation histories, nor large-scale outflows, are required to suppress star formation (e.g., by clearing out all the gas within a local region). Instead, it is enough to have a low, steady level of star formation that prevents the runaway formation of other star-forming clumps. In our model, photoionization (which is modeled in the same way regardless of the preferential direction of the SN feedback) is also partially responsible for star formation regulation in the scale of dwarfs (e.g., see also M. C. Smith et al. 2018).

We may also quantify the efficiency of the stars at generating bulk gas flows via a mass loading factor η, defined as the ratio of the total gas mass expelled by SFR-driven flows, to the total stellar mass formed. For a given run, we calculate

$$\eta = \frac{1}{M_*} \int dt (\dot{M}_{R,\mathrm{Out}} + \dot{M}_{z,\mathrm{Out}}), \qquad (17)$$

where M_* is the total stellar mass formed within the cylinder, and $\dot{M}_{R,\mathrm{Out}}$ and $\dot{M}_{z,\mathrm{Out}}$ are the quantities in Equations (15) and (16) integrated only over outward-moving particles within the shell. The time integral is done over the total simulation time of 2 Gyr. Calculating this value[15] for the three runs pictured in

---

[15] Note that this value should not be compared to typical measurements of the mass loading factors in the literature since we calculate η for a cylinder deeply embedded in the gas disk.
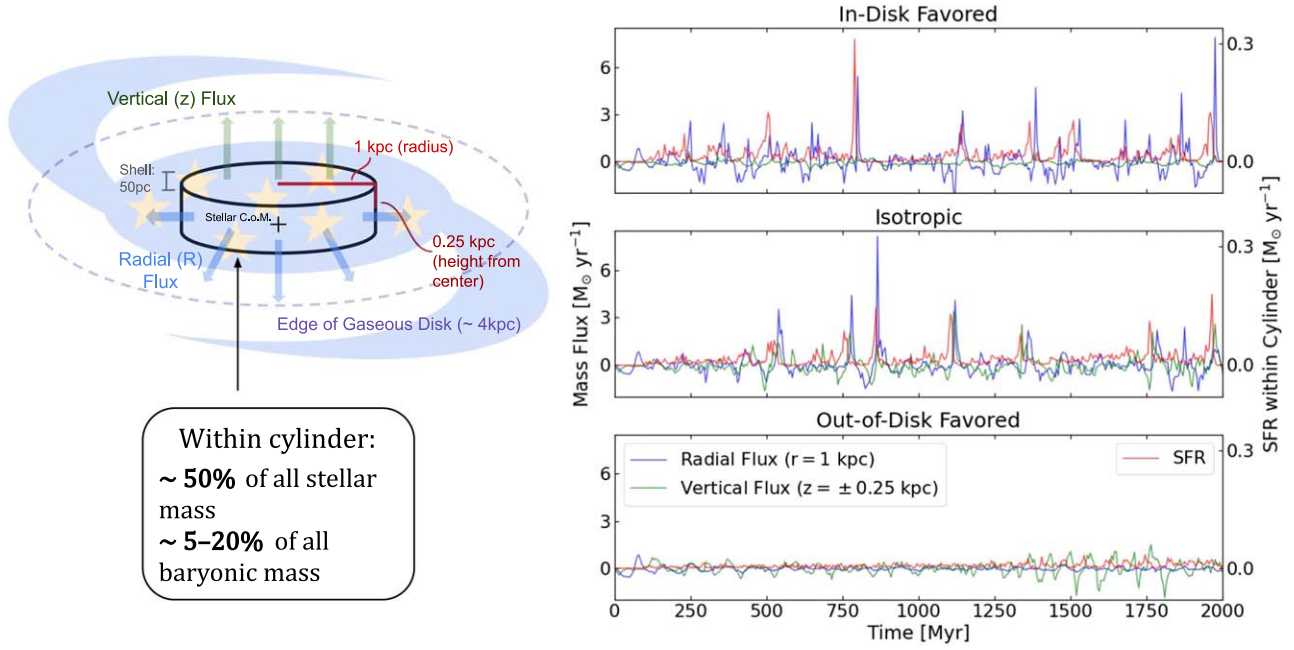
Figure 5. Left: diagram (not to scale) of the cylindrical region of interest, around which the mass flux of the gas is calculated. Right: mass flow history across the boundary of the cylinder of interest, of the in-disk favored (*zeta0.1*, top panel), isotropic (*zeta1*, middle panel), and out-of-disk favored (*zeta10*, bottom panel) runs, and the associated star formation history (red) in the interior of the cylinder. Radial gas flows (Equation (15)) are shown in blue, and vertical flows (Equation (16)) are shown in green. Notably, in the isotropic run, starburst episodes (red peaks) are preceded by a inward bulk gas motion (blue and green dips) followed by peaks of outward motion (blue and green peaks) within the disk, consistent with a more turbulent gas disk. In the in-disk favored run, the vertical gas cycles are suppressed, and in the out-of-disk favored run, the radial gas cycles are suppressed. However, only in the out-of-disk favored run produces bursty star formation and the overall mass flows are suppressed, indicating that radial gas flows are more effective at driving turbulence.
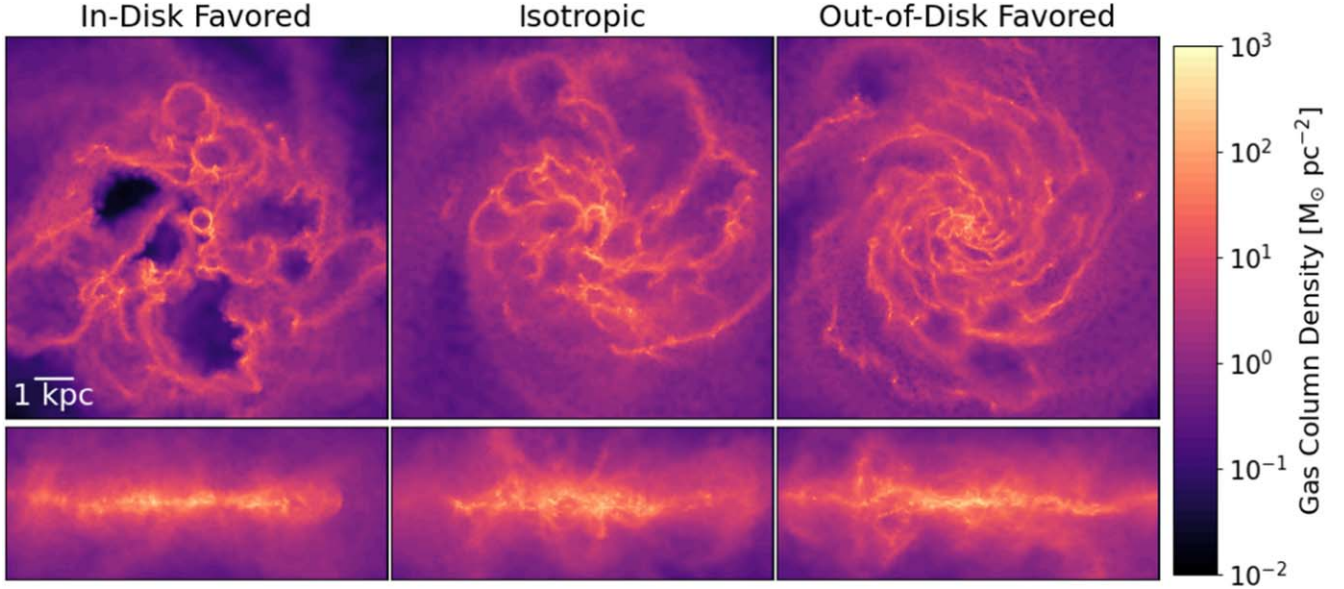
Figure 6. Gas column density of the in-disk favored (left), isotropic (center), and out-of-disk favored (right) runs at snapshot time 1.2 Gyr. The box width of each panel is 10 kpc on a side. Runs with higher injected momentum within the disk exhibit more diffuse structures and larger gas void regions, but slightly less turbulence in the vertical directions, than runs with more injected momentum out of the disk.

Figure 5 yields $\eta \sim 40$ for the in-disk favored run, $\eta \sim 60$ for the isotropic run, and $\eta \sim 80$ for the out-of-disk favored run. This indicates that individual stars in the out-of-disk favored run are more efficient at pushing and driving gas flows than the in-disk favored and isotropic runs. Conversely, the isotropic or in-disk injection models result in increased turbulence within the disk, which is further exacerbated by the momentum

resulting from a larger number of stars formed than in the out-of-disk model.

The effect of the bulk gas motion cycles is further supported by the resulting structure of the gas disk, shown in Figure 6. Significant differences in the structure can be seen as a result of changing the anisotropy factor. In particular, in-disk (*zeta0.1*, left panel) and isotropic (*zeta1*, middle panel) momentum
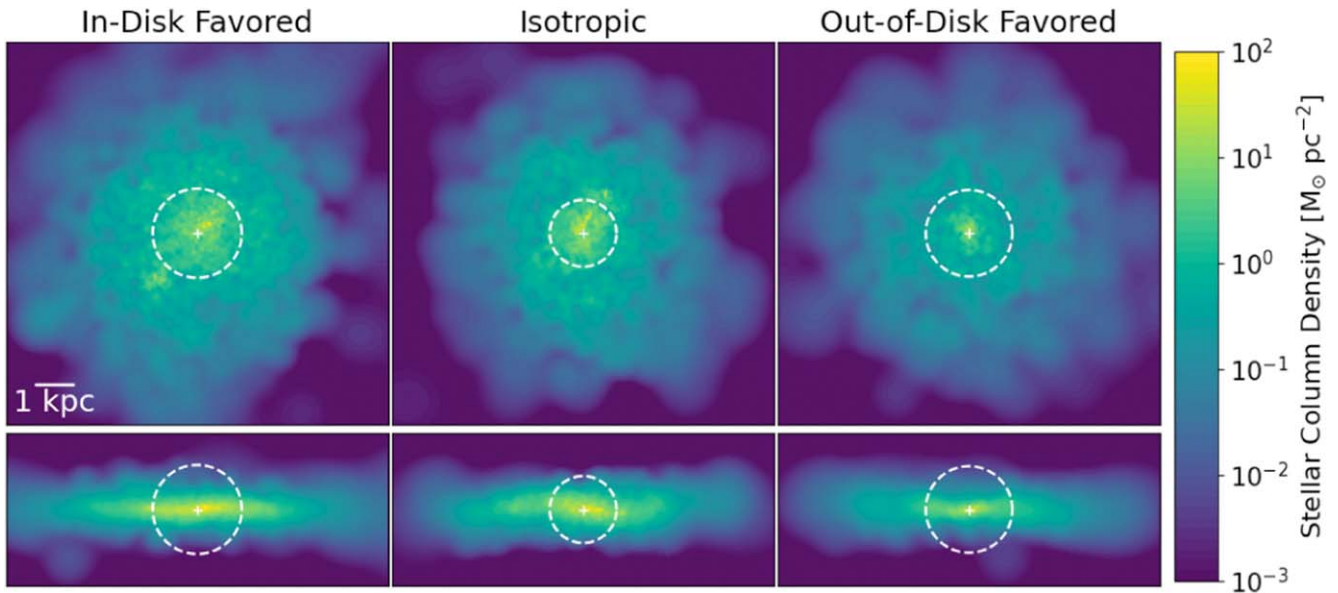
Figure 7. Stellar column density of the in-disk favored (left), isotropic (center), and out-of-disk favored (right) runs for snapshot at 1.2 Gyr. The stellar half-mass radius about the stellar center of mass is shown by the white dashed lines. The box width of each panel is 10 kpc on a side.

injection exhibit a turbulent/disrupted gas morphology, including large regions or bubbles devoid of gas with radius close to ~1 kpc in the most extreme cases. This kind of structure is not present in the case of out-of-disk favored injection (*zeta10*, right panel), which shows a smoother and more regular gas disk without the presence of large gas bubbles.

3.3. Stellar Morphology and Kinematics

The effect of different schemes for SN feedback injection extends also to noticeable changes in the stellar morphology of the simulated dwarf. Previous claims in the literature (e.g., G. S. Stinson et al. 2007; K. El-Badry et al. 2016) have highlighted that bursty star formation histories tend to be associated with a more diffuse distribution of stars, perhaps also contributing to the erasing of age and metallicity gradients in simulated dwarf galaxies (e.g., F. J. Mercado et al. 2021).

To quantify the stellar structure in our simulations, we start by showing projections of the stellar morphology of the in-disk favored (left), isotropic (middle), and out-of-disk favored (right) runs in Figure 7. As a crude measure of how centrally concentrated the stars are in the dwarf, we calculate the stellar half-mass radius r_{half} as the spherical radius from the stellar center of mass in which half of the stellar mass of the galaxy is contained. We show r_{half} as a white dotted circle in each of the panels in Figure 7. r_{half} does not differ significantly between runs (we have explicitly checked this as a function of time) and, in general, the projected stellar structure does not have any obvious indication or trend with the momentum injection model.

However, Figure 8 shows that the kinematics and orbital properties of the stars have an imprint of the chosen feedback injection scheme. We plot, for each simulated galaxy, its velocity dispersion in the 2D radial direction (purple) and the z-direction (green) as a function of its anisotropy factor γ, where the mean value and uncertainty are calculated over all snapshots in the latter 1.5 Gyr of evolution. Preferential injection of momentum in the plane of the disk (lower-γ runs)
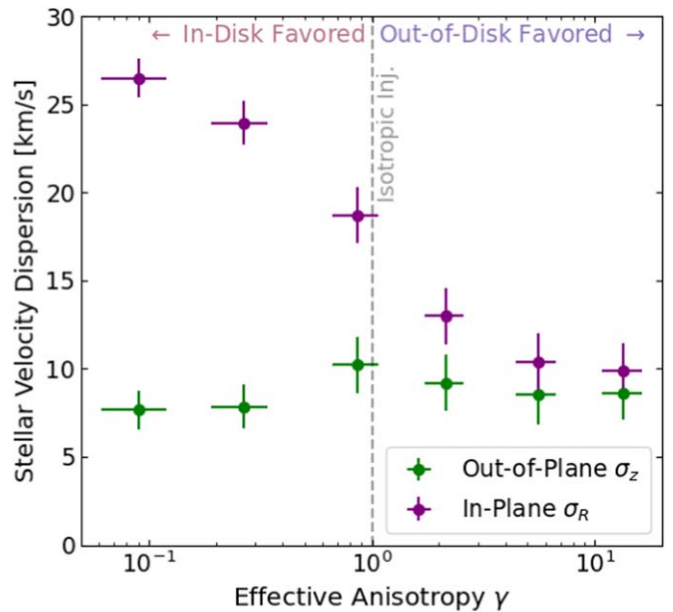

Figure 8. Vertical (green) and in-plane (purple) stellar velocity dispersion of stars as a function of anisotropy. Changing the degree of anisotropy does not affect the vertical velocity dispersion of the stars, even when we inject more momentum in that direction. Conversely, the radial velocity dispersion of stars is inversely correlated with the anisotropy factor, so that higher radial velocity dispersions are observed when the momentum is injected preferentially within the disk. This may occur either as stars tend to be born on more radial trajectories, or as stellar orbits are dynamically heated by radial flows.

results in a noticeably higher stellar radial velocity dispersion, presumably as a combination of two effects: new stars being born from gas with already large radial motions, and the input of dynamical heating to the population of already formed stars as a result of radial flows and compression waves.

Interestingly, the fact that the stellar velocity dispersion in the z-direction shows little to no dependence on γ (green symbols) suggests that stellar kinematics do not always trace the properties of outflowing gas (although they do trace the kinematics of star-forming gas). If, contrarily, newly formed
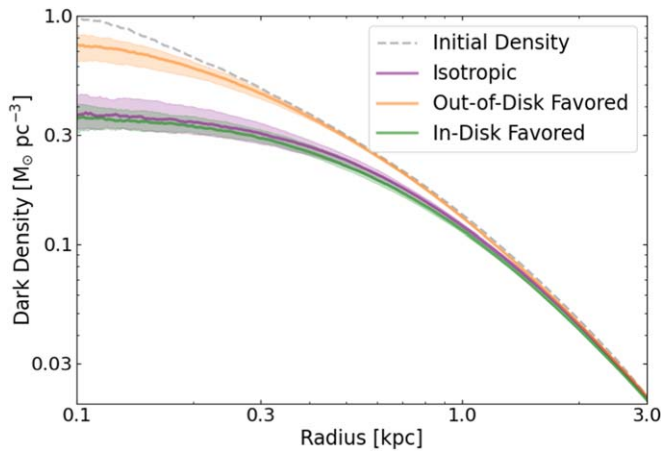
Figure 9. Dark matter density profiles between 1 and 2 Gyr. The median density across snapshots at each radius is plotted as a solid line, and the interquartile range at each snapshot is shaded. Consistent with the understanding of core formation, the out-of-disk favored run, which has a nonbursty star formation history, has a dark matter cusp, and the isotropic and in-disk favored runs, which have bursty star formation histories, have dark matter cores. For comparison, the initial cuspy density profile (measured as the median density from the stellar center of mass over the first 200 Myr, similar across all runs considered) is shown by the gray dashed line.

stars inherited the properties of the bulk gas flow, then the degree of SN anisotropy should affect the stellar kinematics, in the same way that it affects the vertical outflow rates shown in Figure 5. However, this is not the case, as the stellar σ_z appears to be independent of the SN anisotropy; thus, the stellar motions and the total gas motions are not well coupled to each other.

3.4. Distribution of Dark Matter

The difference in the amount and morphology of the bulk gas motions discussed in the previous sections has the potential to impact not only the baryonic morphology of the dwarf, but also its dark matter distribution. Bursty star formation histories that are associated with locally dominant gas expulsion can lead to the transformation of cuspy dark matter halos into lower density dark matter cores (e.g., A. Pontzen & F. Governato 2012; A. Benitez-Llambay et al. 2019). However, models resulting in a smoother star formation history (even when considering the exact same baryonic physics) could in principle preserve the characteristic Lambda cold dark matter (ΛCDM) cuspy profiles, changing the theoretical expectations for dwarf galaxies.

To address this, we compare in Figure 9 the dark matter density profile of our simulated dwarfs in the in-disk favored (*zeta0.1*, green), isotropic (*zeta1*, red) and out-of-disk favored (*zeta10*, orange) runs. These profiles have been calculated as the average dark matter density in the last 1 Gyr to average out temporal fluctuations. Thick lines indicate the median while the shaded regions highlight the interquartile range. We find that lower-γ runs, which are associated with more bursty SFR and in-plane gas flows, tend to have dark matter cores compared to higher-γ runs, for which less bursty SFRs were measured (see Figure 4) and which retain a substantially more cuspy profile. For reference, the dashed gray line indicates the initial profile, which corresponds to a cuspy NFW profile with concentration $c = 15$. This correlation between the mode of star formation

and the inner dark matter distribution is consistent with the expectation from the literature, as discussed above.

Notably, the distinction in the cuspy versus cored dark matter prediction holds when considering exactly the same physics of the ISM. While previous work has already highlighted that some baryonic treatments would result in cores while others would produce cusps (see, e.g., S. Bose et al. 2019) over similar mass ranges, the treatment of the baryons from the models considered was different, opening the possibility that the core formation was purely the result of including more detailed or more realistic star formation and feedback models. This degeneracy is underscored by models resolving SNe directly but not producing cores (T. A. Gutcke et al. 2022a). In short, our results confirm that not only the physics and treatment for the ISM play a role, but even the detailed numerical choices for, e.g., distributing the momentum of the stellar feedback may cause profound changes in the predictions for the density in the inner regions of dwarfs.

This also suggests that implementations of "universal" corrections for modifying the cuspy NFW profile into a lower density core that depend solely on the stellar mass M_* or stellar-to-halo mass ratio M_*/M_{vir} (as proposed, e.g., by A. Di Cintio et al. 2014) might describe the behavior for a given feedback model or family of baryonic models very well, but are not necessarily applicable to others. For example, all runs considered in Figure 9 have a stellar-to-halo mass ratio of $\sim 10^{-2.5}$, a regime where the inner region is predicted to be cored (with a profile slope of -0.3 to -0.1). This is consistent with the isotropic and out-of-disk favored runs at radii below about ~ 500 pc, but the profile slope of the out-of-disk favored run at this distance is nearly -1, consistent with a cusp instead. We hasten to add, however, that this implication regarding universal modifications to the dark matter profile still needs further confirmation from runs within the cosmological setup.

4. Robustness of the Results to Changes in the Cell Weighting Scheme

As stated in Section 2, it is also possible to change the magnitude of the momentum distributed across gas cells by changing the weighting function, as described by the weighting factors w_i. The default cell weighting scheme in SMUGGLE is based on the solid angle subtended by the gas particles from the target star, in a way that nearby cells or cells with a large area have larger weights (see Section 2 in F. Marinacci et al. 2019). This scheme follows other codes that include a similar weighting, like FIRE-2 (P. F. Hopkins et al. 2018b).

However, other choices of the cell weighting scheme are possible, including mass-based and volume-based weighting. In a hydrodynamic solver with roughly equal-mass gas cells, these physically correspond to favoring injection toward dense gas regions and toward diffuse gas regions, respectively (see discussion in P. F. Hopkins et al. 2018b). As the energy-conserving phases of SNe are not explicitly resolved in simulations at our resolution, and because the local environments in which SNe go off are potentially inhomogeneous, it is not immediately clear what gas the feedback momentum will most effectively couple to. As such, the choice of cell weighting scheme should be understood as an assumption made in the subgrid model. In this section, we explore how these three choices (solid angle, volume, and mass) of cell weighting scheme influences the feedback results. The
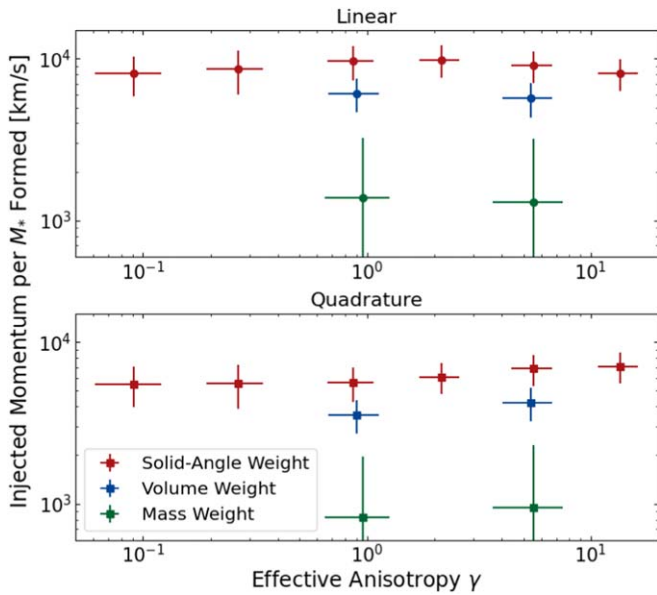
Figure 10. Magnitude of momentum injected by SNe per mass of stars formed, for each run over 2 Gyr. We calculate the total magnitude in two ways: linear (top panel, Equation (19)), and in quadrature (bottom panel, Equation (20)). For the same weighting scheme, there is no dependence of the magnitude of momentum injected on the anisotropy factor γ. However, between solid-angle weighting (red), volume weighting (blue), and mass weighting (green), the magnitude of momentum injected can differ by as much as a factor of ~ 5. These behaviors hold using both calculation methods (although the values do depend on the calculation method).

formulae for these weighting schemes are described in Section 2 (in particular, see Equation (10) and the subsequent discussion).

Nominally, the momentum injected by an SN should be the same across all SN events. However, as discussed in Section 2.2, a number of numerical postprocessing procedures must be applied when imparting the momentum to a neighboring gas cell, to correct for the unresolvedness of the energy-conserving phase. In particular, the momentum going into a gas cell is boosted by the factor β (as per Equation (6), following P. F. Hopkins et al. 2018a), and furthermore, momentum is not added if the gas cell is more than $r_{SB} = 1024$ pc from the star particle. As such, the true amount of momentum injected by star particles depends on the configuration of individual gas cells at the time of the SN event, which can vary across different runs.

In fact, we find that, purely due to these numerical postprocessing effects the momentum typically injected by a single star particle may significantly differ across runs. In particular, the momentum injected by SNe, per stellar mass formed, can vary by almost an order of magnitude when different cell weighting schemes are considered, independent of the anisotropy factor γ in that run. In Figure 10, we plot for each simulation, the mean and standard deviation over all star particles of the quantity

$$\text{Injected Momentum per } M_* = \left(\frac{p_{tot}}{M_{init}}\right)_{stars}, \tag{18}$$

where p_{tot} is the total magnitude of momentum injected by a given star particle, and M_{init} is its initial mass.

Since the injected momentum is a vector quantity, there is no canonical way of calculating its total magnitude. Thus, we

define two possible ways of quantifying p_{tot}: using the linear method

$$p_{tot,Lin.} = \sum_d \sum_{SNe} |\delta p_d|, \tag{19}$$

and the quadrature method

$$p_{tot,Quad.} = \sqrt{\sum_d \left(\sum_{SNe} |\delta p_d|\right)^2}, \tag{20}$$

where δp_d for $d = (x, y, z)$ are the momenta injected during a given SN event in the x-, y-, and z-directions, respectively. Note that this calculation reflects the mean and dispersion normalized by stellar mass formed, so the comparison is meaningful even if the runs formed different amounts of stellar mass by the end. For our default choice, the opening-angle weight (also referred to as the "omega" weight, shown as red symbols), we show that the median input as a function of anisotropy (effective anisotropy, γ) remains quite constant, suggesting that the typical momentum input for this weighting scheme is independent of the directionality (γ) chosen. The trend remains in both, the linear (top panel) or in-quadrature (bottom) measurement of momentum.

We also compare to a volume-weighting scheme (blue) and mass-weighting scheme (green) for the isotropic and out-of-disk momentum injection ($\gamma \sim 1$ and 10, respectively). We have explicitly checked that the effective anisotropy of momentum injection is comparable across all weighting schemes (see Table 2), which then allows for a fair comparison between the total momentum injection at a given γ. Figure 10 shows a systematic shift of the momentum effectively imparted per star depending on the choice of weighting function, with volume-weighting criteria returning values slightly below but comparable to the omega-weighting scheme, but mass-weighted injection results in up to 5 times less momentum input per star. The effect also seems independent of γ, at least for the two explored values here. It is worth noting that of all weighting methods, the opening-angle criteria adopted by default in SMUGGLE seems to maximize the momentum injection into the ISM. Also important is the observation that the choice of cell weighting may be well physically motivated, but can result in unwanted pathological behaviors. For instance, mass-weighting schemes in poorly resolved disks may lead to the creation of artificially large bubbles (P. Torrey et al. 2017), perhaps making such a choice unpreferred for runs with intermediate to low resolution.

These differences in momentum input have a noticeable effect on the star formation histories of our simulated dwarfs. We show the evolution of the star formation history (top) and the total stellar mass (bottom) in Figure 11 for these three weighting schemes, and choosing isotropic momentum injection (left) and out-of-disk injection (right). The SMUGGLE default choice, omega weighted and isotropic momentum injection, leads to the most bursty star formation of all runs (red curve, top left panel).

All weighting schemes seem to self-regulate star formation, at least for the 2 Gyr explored here, with the volume- and mass-weighting models predicting a slight but steady increase of SFR with time. Differences in weighting and directionality of momentum injection can cause variations by factors of 2–3 of the total amount of stars formed, with isotropic injection resulting in systematically larger stellar masses for all
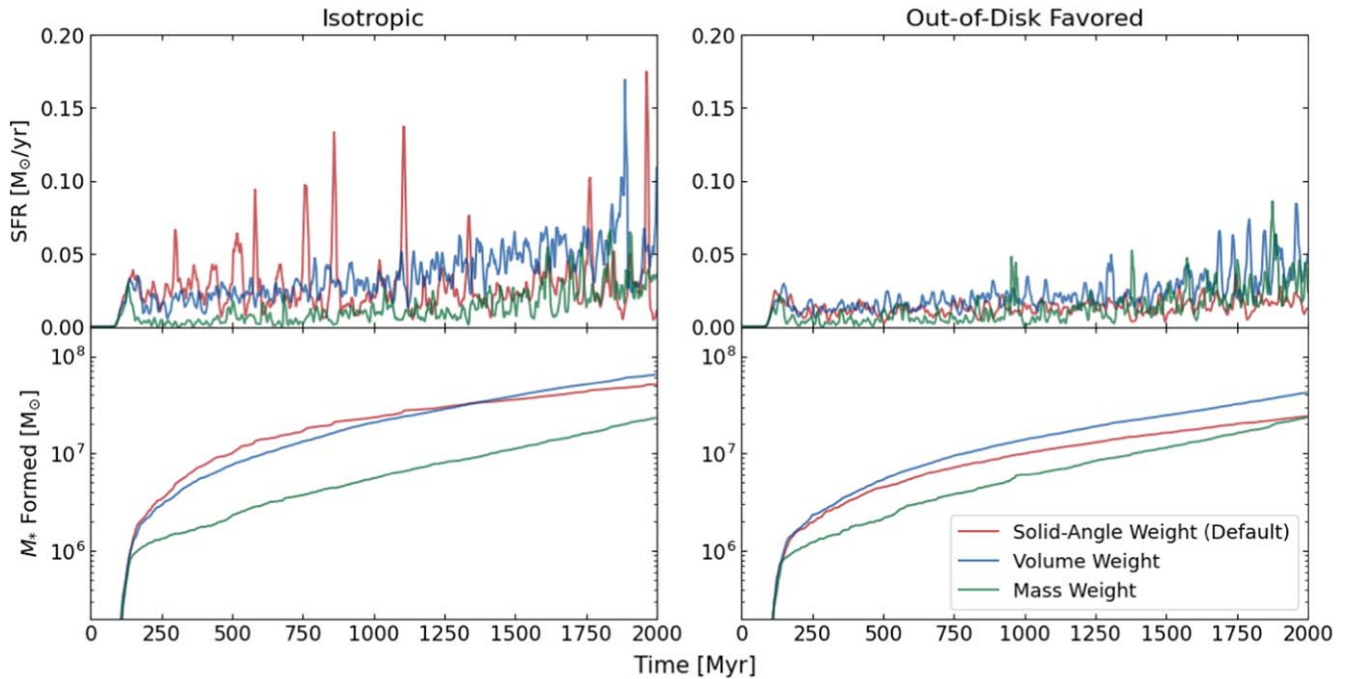
Figure 11. SFR histories (top) and stellar mass formed (bottom) for runs with different weighting schemes: solid angle (red), volume (blue), and mass (green). The left and right panels correspond to isotropic momentum injection ($\gamma \approx 1$) and out-of-disk favored momentum injection ($\gamma > 1$), respectively. In general isotropic injection results on more bursty SFR histories than out-of-disk favored ones. Solid-angle-based criteria assuming isotropic momentum injection maximizes the burstiness of star formation. The total stellar mass formed can vary by factors of 2–3 between runs with different numerical choices.

weighting schemes, while at fixed momentum injection directionality, the mass-weighting scheme results in lower M_*.

Interestingly, neither the total rate of star formation nor the stellar mass are correlated with the magnitude of momentum injected shown in Figure 10. For example, the mass-weighted runs have the least momentum injected per star, but also the lowest rate of star formation, contrary to expectations. Furthermore, the volume-weighted runs form more stars than the omega-weighted runs, but have less momentum injected per star particle than the omega-weighted runs. This shows that the effect of momentum injection on the star formation history is not immediately obvious; that is, it is not true that the input of more feedback momentum translates into more effective suppression of star formation (i.e., a lower stellar mass), as may be naively expected.

5. Conclusions

Undoubtedly, the assumption of isotropy for the momentum deposition resulting from a single SN event in a homogeneous and constant density medium is well justified. However, the ISM of galaxies is far from this idealized constant density assumption, and stellar clustering may cause the overlap and fusion of multiple bubbles leading to a complex system where the assumed isotropy for energy and momentum deposition no longer holds. The scales over which these mechanisms occur are currently underresolved in most galaxy-scale simulations. Here we explored the systematic effects of lifting the hypothesis of isotropic bubble expansion using idealized numerical simulations of an isolated dwarf galaxy run with the SMUGGLE model.

We implemented several different schemes to distribute and couple the momentum resulting from SN feedback onto neighboring gas cells. More specifically, we explored

independently the effects of (i) changing the directionality of the momentum injection (lifting the isotropic assumption) and (ii) studying the effect of different weighting schemes (independent of direction). We label our runs according to the excess of momentum deposited perpendicular to the disk using the parameter γ. Isotropic momentum injection corresponds to $\gamma \approx 1$, while $\gamma > 1$ and $\gamma < 1$ indicate that the momentum injection is favored perpendicular (vertical) and parallel (horizontal) to the plane of the disk, respectively.

We can summarize our most important results as follows.

1. The degree of anisotropy assumed in SN momentum injection greatly affects the burstiness of the star formation history. When momentum is primarily directed perpendicular to the plane of the disk, bursty star formation is suppressed, and fewer total stars are formed, compared to runs in which momentum is primarily injected isotropically or within the plane of the disk.

2. Bursty star formation results from runs where momentum is coupled effectively within the plane of the disk, generating in-plane bulk gas motions that create more turbulence in the disk. The gas structure tends to be more disrupted when momentum is primarily injected within the disk plane, and less disrupted when momentum is primarily injected perpendicular to the disk plane.

3. The anisotropy of the momentum injection also clearly affects the resulting stellar morphology of the dwarf. This can be observed in the 2D radial velocity dispersion of stellar particles being more than double in cases of in-disk favored and isotropic injection compared to an out-of-disk favored momentum injection scheme. Stellar orbits become clearly less circular for models where momentum is primarily coupled in the plane of the disk ($\gamma \lesssim 1$ models), an effect that we may attribute to a combination of higher radial velocities in star-forming gas, and

increased gravitational heating from in-plane gas flows in these runs compared to higher-γ models.

4. Runs with bursty star formation form dark matter cores, and runs with nonbursty star formation retain their dark matter cusps. This is consistent with the existing understanding of the relationship between significant gas flows (typically associated to bursty star formation) and dark matter core formation. However, our results also suggest that in midresolution simulations that rely on subgrid SN feedback prescriptions, the formation of dark matter cores may still depend on the numerical choices. Thus, the core properties such as radial extension and inner density profile are not yet firmly established as a fundamental prediction of the physics included in a given simulation.

5. Different cell weighting schemes in SNe may, due purely to numerical effects, actually lead to different amounts of momentum being injected. This qualitatively changes the star formation history and may vary the total amount of stellar mass formed by factors of 2–3 within 2 Gyr of evolution. A weighting scheme based on opening angle, such as that used in the default version of SMUGGLE, seems to maximize the momentum input per stellar particle, being $\sim$5 times larger than, for example, a scheme based on cell mass alone. As such, the cell weighting scheme must also be understood as a numerical choice (although it may still be a physically motivated choice).

Our results imply that the numerical choices implicit to the subgrid modeling of SN feedback can play a significant role in the predicted properties of simulated dwarf galaxies. In particular, for the SMUGGLE code, we demonstrate that the level of burstiness in the star formation history is particularly sensitive to the numerical implementation of the underlying feedback physics. This has consequences for the predicted stellar and gas morphology, with more bursty runs leading to less rotational support of the gas and stars, along with a more distorted ISM characterized by large bubbles and in-disk gas flows. While the specific effects of the weighting scheme will likely vary from model to model (and depend on the details of the hydrodynamics solver, numerical implementation, etc.), our study is an important reminder that the results from numerical simulations should be scrutinized not only in light of the physics included, but also of the numerical choices made, a subject that receives considerably less attention in the literature.

We stress that, though the parameters studied in this work are numerical, this does not mean that the numerical choices made have no physical correspondence. Indeed, the anisotropy parameter and the cell weighting scheme may be physically motivated choices, which depend on the types of gas that SN explosions are expected to couple to most effectively. In reality, the true nature of how SN momentum couples to ISM gas is not yet well understood, and subgrid models must accurately mimic this coupling in order to produce true predictions from simulations. Thus, in future work it may be instructive to compare these simulations with models that resolve SN explosions explicitly, such as LYRA (T. A. Gutcke et al. 2021, 2022b) and RIGEL (e.g., Y. Deng et al. 2024). In such ultrahigh resolution simulations, details of the momentum distribution, including the degree of anisotropy, are expected to be produced self-consistently by the resolved thermal expansion. Detailed investigations of the bubble morphology in galaxy simulations with resolved SNe might be able to better inform subgrid models that rely on numerical parameters. These parameters may depend on more detailed properties of the ISM such as directional variations in density, in addition to commonly considered zeroth-order parameters such as the energy released or average local density.

A possible interpretation of the results presented here is that the level of burstiness in simulated dwarfs could be overrepresented at least in some galaxy formation models. For example, the lack of formation of dense and compact dwarf galaxies in most codes available today supports the scenario where more violent star formation and feedback cycles are present in simulated dwarfs compared to the real Universe (see the discussion in L. V. Sales et al. 2022). Similarly, as reported by K. El-Badry et al. (2018), simulated dwarfs in FIRE on the scale of $M_* \sim 10^8$–10^9 $M_\odot$ seem less rotationally supported than suggested by H I observations, also consistent with the possibility of too bursty SFRs. In this regard, studies trying to compare the star formation cycles in observations and simulations may prove one of the most important ways to inform dwarf galaxy formation models in simulations (e.g., S. G. Patel et al. 2018; N. Emami et al. 2019, 2021; V. Mehta et al. 2023).

Constraining the star formation cycles is especially important not only for our understanding of dwarf galaxy morphology, but also for the underlying link between bursty star formation histories, gas flows generated, and their impact on the innermost distribution of dark matter in dwarfs. In our runs with less bursty SFR, the formation of dark matter cores at the center of dwarfs was strongly suppressed, meaning that our theoretical expectations of a cusp or a core at the center of the dwarfs depends at least on both, the physics included in the simulation, as well as on the numerical choices made in coarsely implementing this physics in each code.

Appendix
Robustness of the Results to Other Numerical Choices

The changes in the dwarf properties that result from varying the anisotropy of SN momentum injection are robust to changes in the major simulation parameters, including the efficiency and density threshold of star formation, and the mass resolution. To verify this we have run eight additional simulations of the same dwarf, in which these simulation parameters were varied. These runs are summarized in Table 3.

In particular, we find that across a wide range of these parameters, varying the anisotropy factor γ produces the same effect: in-disk favored and isotropic momentum injection produce a bursty SFR history with periods of major in-plane gas motion, whereas out-of-disk favored injection produces a much smoother SFR level with a less turbulent bulk gas flows. We show this behavior in Figure 12.
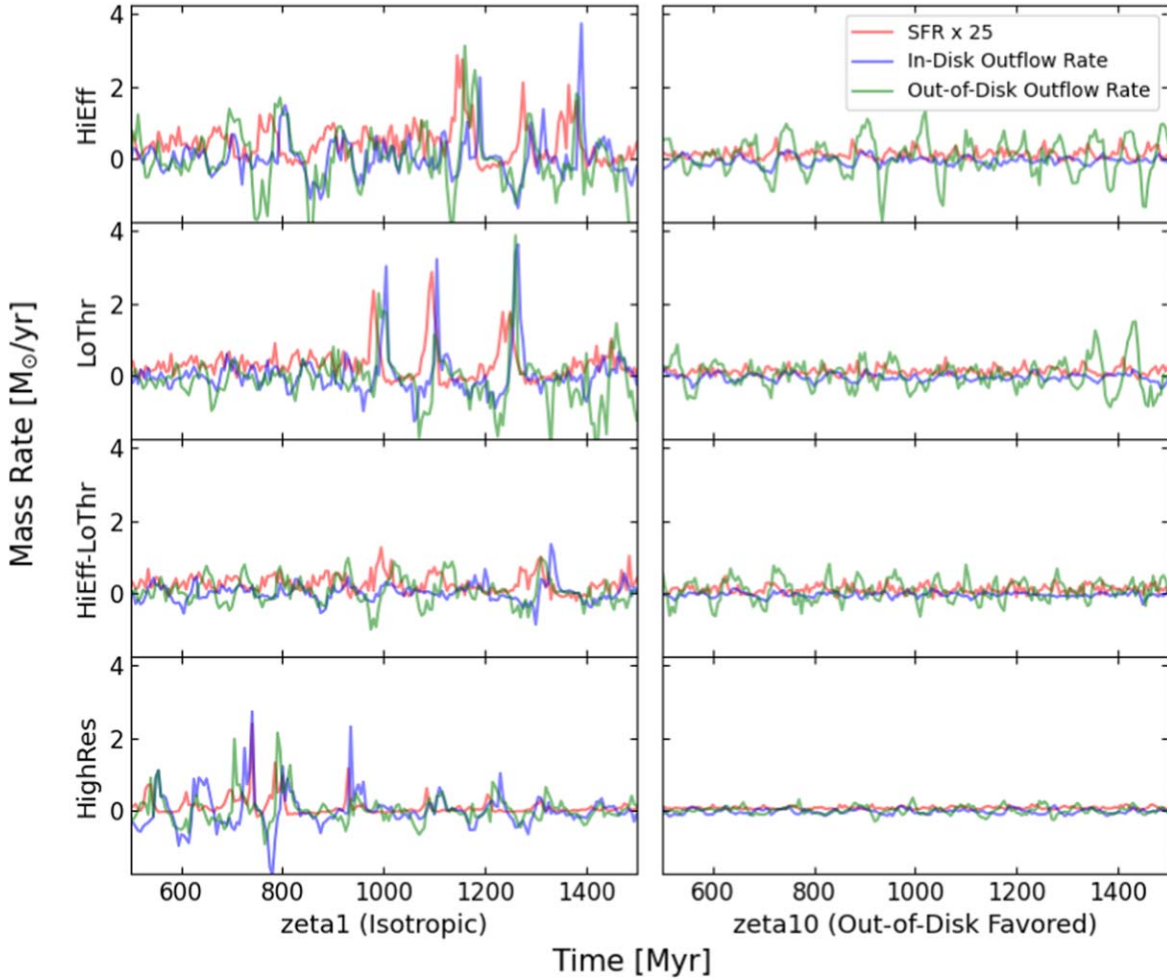
Figure 12. In-disk, or radial (blue) and out-of-disk, or vertical (green), gas flow rate and associated SFR (red) for all eight robustness test runs, with respect to the same cylinder described in Figure 5. In all cases, the *zeta1* runs have burstier SFRs and more violent gas flow patterns, whereas the *zeta10* runs do not. This is the same behavior as observed in the main body of the paper, so changing the anisotropy affects the runs in this way regardless of these numerical choices explored here.

Table 3
List of Simulations Used in Our Robustness Analysis, and the Parameters Used in Each

Simulation Name	Nominal SN Anisotropy ζ	Max. SFR Efficiency	SFR Threshold (m_H cm^{-3})	Target Gas Mass ($M_\odot$)
zeta1-HiEff	1.0	0.9	100	6000
zeta10-HiEff	10.0	0.9	100	6000
zeta1-LoThr	1.0	0.01	1	6000
zeta10-LoThr	10.0	0.01	1	6000
zeta1-HiEff-LoThr	1.0	0.9	1	6000
zeta10-HiEff-LoThr	10.0	0.9	1	6000
zeta1-HighRes	1.0	0.01	100	500
zeta10-HighRes	10.0	0.01	100	500

ORCID iDs

Eric Zhang ⬤ https://orcid.org/0000-0002-7611-8377
Laura V. Sales ⬤ https://orcid.org/0000-0002-3790-720X
Federico Marinacci ⬤ https://orcid.org/0000-0003-3816-7028
Paul Torrey ⬤ https://orcid.org/0000-0002-5653-0786
Mark Vogelsberger ⬤ https://orcid.org/0000-0001-8593-7692
Volker Springel ⬤ https://orcid.org/0000-0001-5976-4599
Hui Li ⬤ https://orcid.org/0000-0002-1253-2763
Rüdiger Pakmor ⬤ https://orcid.org/0000-0003-3308-2420
Thales A. Gutcke ⬤ https://orcid.org/0000-0001-6179-7701

References

Agertz, O., Kravtsov, A. V., Leitner, S. N., & Gnedin, N. Y. 2013, ApJ, 770, 25
Agertz, O., Teyssier, R., & Moore, B. 2010, MNRAS, 410, 1391
Aumer, M., White, S. D. M., Naab, T., & Scannapieco, C. 2013, MNRAS, 434, 3142
Azartash-Namin, B., Engelhardt, A., Munshi, F., et al. 2024, ApJ, 970, 40
Behroozi, P., Wechsler, R. H., Hearin, A. P., & Conroy, C. 2019, MNRAS, 488, 3143
Benitez-Llambay, A., Frenk, C. S., Ludlow, A. D., & Navarro, J. F. 2019, MNRAS, 488, 2387
Bose, S., Frenk, C. S., Jenkins, A., et al. 2019, MNRAS, 486, 4790
Burger, J. D., Zavala, J., Sales, L. V., et al. 2022a, PhRvL, 129, 191103
Burger, J. D., Zavala, J., Sales, L. V., et al. 2022b, MNRAS, 513, 3458
Cenci, E., Feldmann, R., Gensior, J., et al. 2023, MNRAS, 527, 7871
Chabrier, G. 2003, PASP, 115, 763
Chaikin, E., Schaye, J., Schaller, M., et al. 2022, MNRAS, 514, 249
Chaikin, E., Schaye, J., Schaller, M., et al. 2023, MNRAS, 523, 3709
Chevalier, R. A. 1974, ApJ, 188, 501
Cioffi, D. F., McKee, C. F., & Bertschinger, E. 1988, ApJ, 334, 252
Conroy, C., & Wechsler, R. H. 2009, ApJ, 696, 620
Dalla Vecchia, C., & Schaye, J. 2012, MNRAS, 426, 140
Deng, Y., Li, H., Liu, B., et al. 2024, arXiv:2405.08869
Di Cintio, A., Brook, C. B., Macciò, A. V., et al. 2014, MNRAS, 437, 415
Draine, B. T., & Woods, D. T. 1991, ApJ, 383, 621
Dutton, A. A., Macciò, A. V., Dekel, A., et al. 2016, MNRAS, 461, 2658
El-Badry, K., Bradford, J., Quataert, E., et al. 2018, MNRAS, 477, 1536
El-Badry, K., Ostriker, E. C., Kim, C.-G., Quataert, E., & Weisz, D. R. 2019, MNRAS, 490, 1961
El-Badry, K., Wetzel, A., Geha, M., et al. 2016, ApJ, 820, 131
Emami, N., Siana, B., El-Badry, K., et al. 2021, ApJ, 922, 217
Emami, N., Siana, B., Weisz, D. R., et al. 2019, ApJ, 881, 71
Emerick, A., Bryan, G. L., & Mac Low, M.-M. 2019, MNRAS, 482, 1304
Freundlich, J., Dekel, A., Jiang, F., et al. 2020, MNRAS, 491, 4523
Gatto, A., Walch, S., Naab, T., et al. 2016, MNRAS, 466, 1903
González-Samaniego, A., Colín, P., Avila-Reese, V., Rodríguez-Puebla, A., & Valenzuela, O. 2014, ApJ, 785, 58
Guedes, J., Callegari, S., Madau, P., & Mayer, L. 2011, ApJ, 742, 76
Gutcke, T. A., Pakmor, R., Naab, T., & Springel, V. 2021, MNRAS, 501, 5597
Gutcke, T. A., Pakmor, R., Naab, T., & Springel, V. 2022a, MNRAS, 513, 1372
Gutcke, T. A., Pfrommer, C., Bryan, G. L., et al. 2022b, ApJ, 941, 120

Hernquist, L. 1990, ApJ, 356, 359
Hopkins, P. F. 2024, arXiv:2404.16987
Hopkins, P. F., Quataert, E., & Murray, N. 2011, MNRAS, 417, 950
Hopkins, P. F., Wetzel, A., Kereš, D., et al. 2018a, MNRAS, 477, 1578
Hopkins, P. F., Wetzel, A., Kereš, D., et al. 2018b, MNRAS, 480, 800
Hopkins, P. F., Wetzel, A., Wheeler, C., et al. 2023, MNRAS, 519, 3154
Hu, C.-Y. 2019, MNRAS, 483, 3363
Jahn, E. D., Sales, L. V., Marinacci, F., et al. 2023, MNRAS, 520, 461
Karpov, P. I., Martizzi, D., Macias, P., et al. 2020, ApJ, 896, 66
Katz, N. 1992, ApJ, 391, 502
Keller, B. W., Wadsley, J., Benincasa, S. M., & Couchman, H. M. P. 2014, MNRAS, 442, 3013
Kim, C.-G., & Ostriker, E. C. 2015, ApJ, 802, 99
Krumholz, M. R., & Tan, J. C. 2007, ApJ, 654, 304
Lahén, N., Naab, T., Johansson, P. H., et al. 2020, ApJ, 891, 2
Larson, R. B. 1974, MNRAS, 169, 229
Li, C., Li, H., Cui, W., et al. 2024, MNRAS, 529, 4073
Marinacci, F., Sales, L. V., Vogelsberger, M., Torrey, P., & Springel, V. 2019, MNRAS, 489, 4233
Martizzi, D., Faucher-Giguere, C.-A., & Quataert, E. 2015, MNRAS, 450, 504
Mehta, V., Teplitz, H. I., Scarlata, C., et al. 2023, ApJ, 952, 133
Mercado, F. J., Bullock, J. S., Boylan-Kolchin, M., et al. 2021, MNRAS, 501, 5121
Mihos, J. C., & Hernquist, L. 1994, ApJL, 425, L13
Moster, B. P., Naab, T., & White, S. D. M. 2013, MNRAS, 428, 3121
Murante, G., Monaco, P., Giovalli, M., Borgani, S., & Diaferio, A. 2010, MNRAS, 405, 1491
Navarro, J. F., Eke, V. R., & Frenk, C. S. 1996a, MNRAS, 283, L72
Navarro, J. F., Frenk, C. S., & White, S. D. M. 1996b, ApJ, 462, 563
Navarro, J. F., & White, S. D. M. 1993, MNRAS, 265, 271
Patel, S. G., Kelson, D. D., Diao, N., Tonnesen, S., & Abramson, L. E. 2018, ApJL, 866, L21
Pittard, J. M. 2019, MNRAS, 488, 3376
Pontzen, A., & Governato, F. 2012, MNRAS, 421, 3464
Read, J. I., Agertz, O., & Collins, M. L. M. 2016, MNRAS, 459, 2573
Sales, L. V., Navarro, J. F., Schaye, J., et al. 2010, MNRAS, 409, 1541
Sales, L. V., Wetzel, A., & Fattahi, A. 2022, NatAs, 6, 897
Scannapieco, C., Wadepuhl, M., Parry, O. H., et al. 2012, MNRAS, 423, 1726
Sedov, L. I. 1959, Similarity and Dimensional Methods in Mechanics (New York: Academic)
Smith, M. C., Bryan, G. L., Somerville, R. S., et al. 2021, MNRAS, 506, 3882
Smith, M. C., Sijacki, D., & Shen, S. 2018, MNRAS, 478, 302
Sparre, M., Hayward, C. C., Feldmann, R., et al. 2017, MNRAS, 466, 88
Springel, V. 2010, MNRAS, 401, 791
Springel, V., & Hernquist, L. 2003, MNRAS, 339, 289
Stinson, G., Seth, A., Katz, N., et al. 2006, MNRAS, 373, 1074
Stinson, G. S., Dalcanton, J. J., Quinn, T., Kaufmann, T., & Wadsley, J. 2007, ApJ, 667, 170
Taylor, G. I. 1950, RSPSA, 201, 159
Teyssier, R., Pontzen, A., Dubois, Y., & Read, J. I. 2013, MNRAS, 429, 3068
Thornton, K., Gaudlitz, M., Janka, H. T., & Steinmetz, M. 1998, ApJ, 500, 95
Tollet, E., Macciò, A. V., Dutton, A. A., et al. 2016, MNRAS, 456, 3542
Torrey, P., Hopkins, P. F., Faucher-Giguere, C.-A., et al. 2017, MNRAS, 467, 2301
Vogelsberger, M., Genel, S., Sijacki, D., et al. 2013, MNRAS, 436, 3031
Vogelsberger, M., Marinacci, F., Torrey, P., & Puchwein, E. 2020, NatRP, 2, 42